Journal of ELECTRONIC MATERIALS, Vol. 47, No. 7, 2018
https://doi.org/10.1007/s11664-018-6171-3

Synthesis and Characterization of Ferromagnetic Fe_3O_4–ZnO Hybrid Core–Shell Nanoparticles

K.K. NISHAD,[1] NEHA TIWARI,[2] and R.K. PANDEY[3,4]

1.—Department of Nanoscience and Technology, University of Calicut, Malappuram, Kerala 673635, India. 2.—School of Electronics Engineering, NIIT University, Neemrana, Rajasthan 301705, India. 3.—Department of Physics, Barkatullah University, Bhopal, MP 462026, India. 4.—e-mail: prof.rkpandey@gmail.com

Room-temperature synthesis of multifunctional core–shell nanostructures with iron oxide (Fe_3O_4) core and zinc oxide (ZnO) shell is described. High-resolution transmission electron microscopy revealed the occurrence of heteroepitaxial growth of a ZnO shell over the iron oxide nanoparticle core. The formation of the core–shell nanostructure was also evidenced by x-ray diffraction and x-ray photoelectron spectroscopy analyses. The core Fe_3O_4 nanoparticles exhibited superparamagnetic behavior at room temperature in an externally applied magnetic field. However, magnetic measurements of the core–shell nanoparticles revealed ferromagnetic behavior, originating from defect-induced ferromagnetism in the ZnO shell. The prepared core–shell nanoparticles also exhibited strong photoresponse while retaining ferromagnetic behavior at room temperature.

Key words: Fe_3O_4–ZnO, core–shell, ferromagnetic nanostructures, superparamagnetism, photoluminescence

INTRODUCTION

Multifunctional nanoparticles, utilizing two or more materials as constituents, are of considerable research interest for *in vivo* imaging, early detection of cancer, drug delivery, etc. Colloidal magnetic nanoparticles exhibiting superparamagnetism, high coercivity, low Curie temperature, and high magnetic susceptibility provide a suitable platform for preparation of such multifunctional nanomaterials[1–4] when the magnetic property is to be combined with another desired property. Amongst known magnetic materials, nanoparticles of iron oxide (Fe_3O_4) exhibit superparamagnetism when the particle size becomes less than 16 nm.[5–7]

The toxicity of iron oxide nanoparticles, however, increases as the particle size is reduced, limiting the utility of bare nanometer-sized magnetic particles in biomedical applications. Suitable overcoating of magnetic nanoparticles is therefore required to overcome these limitations. We chose overcoating with zinc oxide (ZnO) to form a shell over the iron oxide core structure as a model system in the present study. ZnO is a direct-bandgap (3.36 eV) material with large exciton binding energy ($\sim$ 60 meV),[8–10] exhibiting intense visible emission in the blue–green region, and has much technological promise for use in fluorescence imaging. Moreover, since it is a nontoxic material, great interest is emerging in its use for biosensing, imaging, and cancer detection.[11] Hanley et al.[12] reported that ZnO nanoparticles exhibit strong preferential ability to kill cancerous T cells compared with normal cells. Such novel properties including selective toxicity towards disease-causing cells indicate the potential utility of ZnO nanoparticles in treatment of cancer and autoimmunity.

Successive hybrid growth of an inorganic luminescent material on iron oxide magnetic nanoparticles also promises multifunctionality for application in medical diagnostics, drug delivery, spintronics, and photon-induced magnetic devices.[13–20] However, very few reports on investigations of such multifunctional core–shell nanoparticles have been

(Received August 2, 2017; accepted February 22, 2018; published online March 8, 2018)

published. Recently, some reports on successful and controllable synthesis of magnetic–luminescent core–shell nanoparticle were published. Chiu et al.[21] synthesized Fe_3O_4–ZnO core–shell nanocrystals using thermal pyrolysis of zinc acetate on the surface of Fe_3O_4 nanoparticles. Kwon et al.[22] reported synthesis of Fe_3O_4–CdS heterostructures using a high-temperature route. Developing a room-temperature, wet synthesis route for such hybrid nanostructures would prove to be technologically more advantageous. Previously, room-temperature solution-phase synthesis of Fe_3O_4-CdS hybrid core–shell nanoparticles was reported by Joseph et al.[13] We successfully extended this work for room-temperature growth of Fe_3O_4–ZnO core–shell nanostructures. Another significant result reported herein is the weak ferromagnetic behavior of the as-synthesized core–shell structure, in contrast to the superparamagnetic behavior reported by other researchers.[22]

EXPERIMENTAL PROCEDURES

Preparation of Fe_3O_4 Nanoparticles

Alkaline coprecipitation of Fe(III) and Fe(II) salts in aqueous media is the most universally adopted synthetic approach to produce iron oxide nanoparticles, due to its versatility, low cost, feasibility for scale-up, and hydrophilic surface character of the products. Room-temperature synthesis of Fe_3O_4 nanoparticles was carried out using aqueous solution of ferrous and ferric chloride at molar ratio of 1:2. Ammonia was used as precipitating agent, maintaining pH 11 during synthesis. The reaction of magnetite in aqueous medium can be written as

$$2Fe^{3+} + Fe^{2+} + 8OH^- \rightarrow Fe_3O_4 + 4H_2O \qquad (1)$$

All reagents used were of analytical reagent (AR) grade. Particle size was controlled using an appropriate concentration of mercaptoethanol. Three samples of Fe_3O_4 nanoparticles, viz. F1 (9 nm), F2 (7.3 nm), and F3 (5.4 nm), were synthesized using different mercaptoethanol concentrations of 0.0 M, 0.005 M, and 0.0225 M, respectively.

Preparation of Fe_3O_4–ZnO Core–Shell Nanoparticles

Growth of ZnO on Fe_3O_4 nanoparticles was accomplished in a reaction matrix using zinc acetate (ZnAc) and sodium hydroxide (NaOH) in absolute ethanol at room temperature. All chemicals were of AR grade. The molar concentration of ZnAc precursor was determined by first calculating the number of ZnO molecules required to coat the Fe_3O_4 nanoparticle surface. Based on x-ray diffraction (XRD) analysis and transmission electron microscopy (TEM) measurements, the core Fe_3O_4 nanoparticles were assumed to be spherical with diameter of 5.4 nm. To coat the Fe_3O_4 core structure with a shell layer a few nanometers thick, the molar concentration of zinc acetate was kept at 0.01 M. The molar ratio of ZnAc to NaOH was 1:2, and the total volume was set as 30 mL. Freshly synthesized Fe_3O_4 core nanoparticles (0.1 mg) were injected into the reaction matrix under vigorous stirring. As-prepared Fe_3O_4 nanoparticle samples F1, F2, and F3 were used as cores, on which the ZnO shell was allowed to grow for predetermined duration of 20 min, obtaining a set of three core (Fe_3O_4)–shell (ZnO) samples, designated as FZ1, FZ2, and FZ3, respectively. Using high-resolution TEM, the thickness of the shell was estimated to be approximately 2.3 nm for all samples. The as-grown core–shell structures were quickly removed from the bath using magnetic separation and washed thoroughly in ethanol followed by methanol.

XRD patterns were recorded in thin-film grazing-angle mode using XRD-6000 (Shimadzu, Japan) powder diffractometer using Cu K_α line. Beam divergence was restricted with the help of a 0.15-mm slit on the source side. Drive axis of 2 was used in the scan range between 16° and 70° at 1°/min with step size of 0.002°. The instrumental propagation error in the d-value was $\pm$ 0.003 Å. Since, Fe_3O_4 and ZnO crystals possess lattice planes with approximately similar d spacings, the experimentally obtained structural data were further refined using Rietveld refinement using the FullProf software program (version 3.5 LLB-JRC). In the first step of the refinement, the global parameters (2θ-zero, instrumental profiles including profile asymmetry, background, and specimen placement) were refined. In the next step, the structure parameters (lattice parameters, atomic coordinates, specimen profile, breadth parameter, preferred orientation, and site occupancy) were refined in sequential mode. In the last cycle, when the discrepancy factor reached its minimum value, all the parameters (global and structural) were refined simultaneously, giving the goodness of fit.

For structural and particle size analysis, transmission electron microscopy (TEM) was also employed. For TEM, samples of nanoparticles were prepared by dispersion into ethanol followed by ultrasonication for 1 h. The ultrasonicated suspension was further diluted. One drop of this suspension was loaded onto a carbon-coated grid and dried prior to TEM examination. For TEM observations, a J 1210 JEOL TEM operating at 300 kV was used in imaging as well as diffraction mode.

For atomic force microscopy (AFM) analysis, thin films of Fe_3O_4–ZnO core–shell nanoparticles were deposited by spin-coating onto precleaned glass substrate. Morphological characteristics of the core–shell films were studied by AFM (model SPM9500J2, Shimadzu, Japan), using a 55 μm × 55 μm piezoscanner with vertical z-axis resolution of 0.1 nm in contact mode. Imaging was carried out with 20-nm-wide legged silicon nitride cantilevers. Magnetic force microscopy (MFM)

imaging was carried out using the same microscope with Co/Cr-covered cantilevers having normal spring constant of 2 N/m. Before scanning, the cantilevers were magnetized using a small magnet. The MFM image was taken in lift mode at lift height of 100 nm.

Optical absorption spectra of the samples were recorded by dual-beam ultraviolet–visible (UV–Vis) spectrophotometer (UVPC 1601, Shimadzu) at spectral bandwidth of 2 nm. A computer-controlled rationing luminescence spectrophotometer LS55 (PerkinElmer Instruments, UK) with $\lambda_{accuracy} = \pm 1.0$ nm and $\lambda_{reproducibility} = \pm 0.5$ nm was used for photoluminescence studies.

X-ray photoelectron spectroscopy (XPS) was employed for analysis of the composition profile using an ESCALAB (BSW, UK) spectrometer fitted with a concentric hemispherical electron energy analyzer and Al K_α source ($h\nu$ = 1486.6 eV). *In situ* cleaning and sputtering during acquisition of data was performed using an argon ion gun equipped in the analysis chamber. All analyses were performed under ultrahigh-vacuum condition at base pressure of 1.33×10^{-11} kPa. The photoelectron signal after amplification was recorded with the help of an *X*–*Y* recorder. All observed elemental peaks were referred to the C 1*s* electron peak at 284.6 eV as internal standard.

The magnetization of Fe_3O_4 nanoparticles and Fe_3O_4–ZnO core–shell samples was measured as a function of the applied magnetic field H using a MPMS superconducting quantum interference device (SQUID) magnetometer. The hysteresis response of the nanoparticles was recorded by varying H between 7 T and 1.5 T at 300 K.

RESULTS AND DISCUSSION

Structural Characterization

Figure 1a shows the observed XRD spectra of a typical as-prepared ZnO nanoparticle sample used in this study for growth of the shell layer. The XRD pattern of the ZnO nanoparticles exhibited seven peaks located at 2θ = 31.66°, 34.40°, 36.14°, 47.50°, 56.56°, 62.76°, and 67.93°, corresponding to (100), (002), (101), (102), (110), (103), and (112) planes of wurtzite phase of ZnO. The average particle size of the as-prepared sample was calculated using Scherrer's broadening formula to be 7.3 nm.

The XRD patterns of Fe_3O_4 nanoparticles as synthesized using increasing mercaptoethanol concentrations are also shown in Fig. 1b, c, and d for sample F1 to F3, respectively. These nanoparticles were used as the core for growth of Fe_3O_4–ZnO core–shell nanostructures. The XRD profiles observed for all the Fe_3O_4 samples displayed several relatively strong reflections lying between 2θ value of 28° to 80°. All the observed XRD peaks could be assigned to (220), (311), (400), (422), (511), and (440) planes of cubic spinal phase of Fe_3O_4.

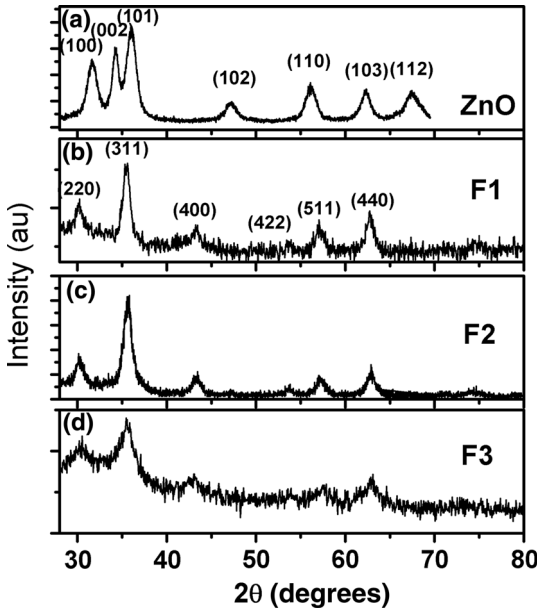

Fig. 1. Observed x-ray diffraction spectra of as-synthesized (a) ZnO and Fe_3O_4 core samples, (b) F1, (c) F2, and (d) F3.

Systematic line width broadening with increasing surfactant concentration is clearly observed in Fig. 1b–d, suggesting concomitant reduction in particle size with increasing mercaptoethanol concentration employed during synthesis of the nanocrystalline Fe_3O_4 samples F1 to F3. Comparison of the experimentally observed peak intensities with corresponding standard values also indicated preferred growth of (311) plane. The most prominent (311) peak was used to estimate the mean particle size using the Scherrer formula, yielding values of 9.0 nm, 7.3 nm, and 5.4 nm for F1, F2, and F3, respectively.

Figure 2 depicts the XRD pattern observed for the Fe_3O_4–ZnO core–shell nanoparticle samples FZ1, FZ2, and FZ3. The core nanoparticle sizes used were 9.0 nm (F1), 7.3 nm (F2), and 5.4 nm (F3), respectively. The XRD spectrum for sample FZ1 mainly consisted of six peaks situated at 2θ = 30.04°, 35.43°, 43.12°, 53.51°, 57.06°, and 62.86°. The XRD results reveal some very interesting features. In all the samples FZ1, FZ2, and FZ3, the observed peak positions nearly match with the corresponding positions for the Fe_3O_4 core samples F1, F2, and F3, respectively. However, the peak widths decreased in all cases compared with the corresponding core nanoparticles. This is indeed surprising. To seek a possible explanation, it is necessary to recall that zinc (being more electropositive) can displace iron atoms on the surface during the initial stage of shell growth, effectively decreasing the size of the Fe_3O_4 core. The two coexisting core–shell phases with lattice planes having similar d spacing will be seen as one crystalline structure, hence the diffraction peaks will become narrower compared with the peaks observed for the core nanoparticles.

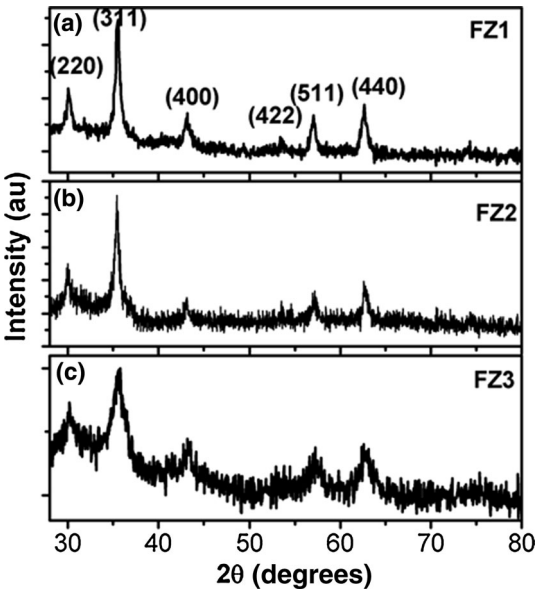

Fig. 2. X-ray diffraction spectra observed for as-synthesized Fe_3O_4–ZnO core–shell samples (a) FZ1, (b) FZ2, and (c) FZ3.

This coexistence of the closely matching lattices of Fe_3O_4 and ZnO therefore results in a strain-free core–shell interface and hence heteroepitaxial growth of the shell layer, forming a coincidental lattice structure.

Transmission Electron Microscopy (TEM)

To investigate the particle size and morphology of the Fe_3O_4 core sample, we employed high-resolution TEM. As-prepared iron oxide nanoparticles were suspended in water and placed on a carbon-coated copper grid for electron microscopy analysis. A TEM image and selected-area diffraction pattern of Fe_3O_4 sample F2 are shown in Fig. 3. The TEM image reveals homogeneous spherical nanoparticles. Due to the extremely small particle size, the concomitant high specific area, and their intrinsic superparamagnetic nature, many nanoparticles formed larger agglomerates.

The average particle size of the nanoparticles was estimated as ~ 7.2 nm ($\pm$ 1.0 nm), in good agreement with the XRD result. The size distribution histogram of the Fe_3O_4 nanoparticles is shown in the inset of Fig. 3a. The selected-area electron diffraction (SAED) pattern revealed characteristic circular diffraction patterns corresponding to (220), (311), (400), (511), and (440) planes of cubic phase of Fe_3O_4.

Figure 4a shows a TEM image of as-prepared Fe_3O_4–ZnO core–shell nanoparticle sample FZ2. A high-resolution image of the lattice planes for Fe_3O_4 and ZnO is shown in Fig. 4b. The measured lattice fringe distances of 0.30 nm and 0.28 nm correspond to (220) plane of Fe_3O_4 and (100) plane of ZnO, respectively. The observation of clear lattice fringes also implies relatively strain-free growth of the interface with good crystallinity.

The lattice mismatch between $d_{(220)}$ of Fe_3O_4 and $d_{(100)}$ of ZnO was calculated using the equation

$$\mathrm{MM}_{hkl} = \left[\frac{d_{hkl}(\mathrm{Fe_3O_4}) - d_{hkl}(\mathrm{ZnO})}{d_{hkl}(\mathrm{Fe_3O_4})}\right], \qquad (2)$$

where MM_{hkl} is the Miller plane mismatch and d_{hkl} is the interplanar distance. The Miller plane mismatch between (220) of Fe_3O_4 and (100) plane of ZnO was small, calculated to be 0.06. This small lattice mismatch is responsible for the heteroepitaxial growth of the ZnO shell on the Fe_3O_4 core nanoparticles.

X-ray Photoelectron Spectroscopy (XPS)

X-ray photoelectron spectroscopy (XPS) analysis was performed for compositional analysis and to determine the chemical state of the constituent elements in ZnO, Fe_3O_4 (sample F2), and Fe_3O_4–ZnO core–shell nanoparticles (sample FZ2). All elemental peaks were referred to the C 1*s* photoelectron peak at 284.6 eV as internal standard. The wide-scan spectra for the ZnO sample, core sample F2, and core–shell sample FZ2 are shown in Fig. S1a, b, and c, respectively, in the Electronic Supplementary Material.

Figure 5a, b, and c shows the narrow-scan O 1*s* spectra recorded for the ZnO, Fe_3O_4 (F2), and corresponding core–shell sample FZ2, respectively. The shape of the O 1*s* spectrum for all the samples was asymmetric, indicating contributions from several components. To provide deeper insight, the O 1*s* spectra were deconvoluted assuming Gaussian line shape, and the results are shown in Fig. 5d, e, and f for ZnO, F2, and FZ2 samples, respectively. The O 1*s* spectrum for the ZnO sample could be deconvoluted into three peaks (Oa, Ob, and Oc), as shown in Fig. 5d. The first peak (Oc) located at 530.0 eV matches well with the standard binding energy value for crystalline oxygen in ZnO.[23,24] The peak located at 531.5 eV (Ob) may originate from oxygen in the vicinity of oxygen vacancy sites.[25] The origin of the peak Oa (532.0 eV) may be ascribed to the presence of chemisorbed oxygen in ZnO. The O 1*s* peak for Fe_3O_4 sample F2 could be deconvoluted into two distinct peaks at 530.0 eV and 532.0 eV, designated as O_{Fc} and O_{Fa}, respectively. The former peak (O_{Fc}) matches with that for crystalline oxygen in Fe_3O_4 crystal.[23] The latter peak (O_{Fa}) may originate from oxygen species chemisorbed on the nanoparticle surface.

It is interesting to note that the shape of the O 1*s* binding energy peak for the core–shell sample (FZ2) was markedly different from the corresponding peaks observed for the ZnO and F2 samples. The O 1*s* binding energy peak of the core–shell sample FZ2 could be deconvoluted into three peaks at 530.0 eV (Oc), 531.5 eV (Ob), and 532 eV (Oa), as

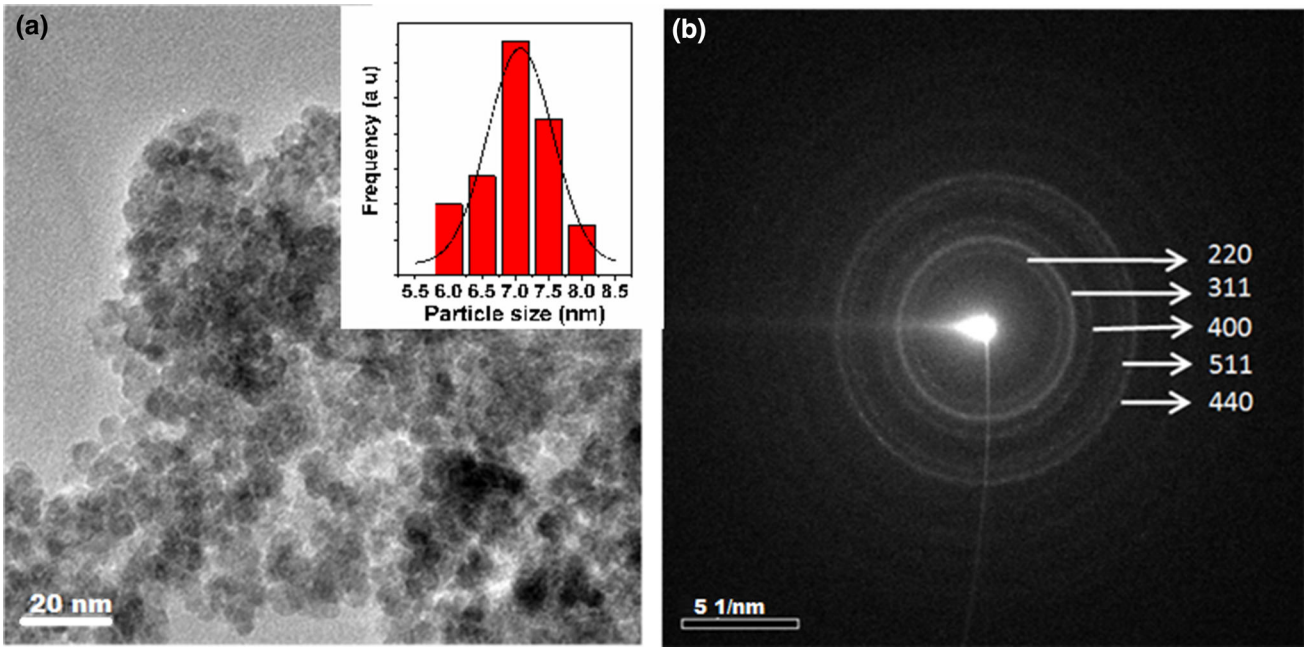

Fig. 3. (a) TEM image and (b) SAED pattern of Fe_3O_4 nanoparticles (sample F2) grown using mercaptoethanol concentration of 0.005 mol. The size distribution histogram is given in (a).

shown in Fig. 5f. The first peak, designated as Oc (530.0 eV), was also observed for Fe_3O_4 as well as ZnO and hence can be attributed to crystalline oxygen present in both or either phase. The second deconvoluted peak (Ob, 531.5 eV) could be observed in the O 1*s* spectrum for ZnO (Fig. 5d) but not in the corresponding O 1*s* spectrum (Fig. 5e) for Fe_3O_4. Hence, this peak may be assigned to presence of oxygen in vicinity of oxygen vacancies in ZnO. The third deconvoluted peak (Oa at 532.0 eV) in Fig. 5f matches with chemisorbed oxygen.

Figure 6a shows a typical narrow-scan Zn 2*p* photoelectron spectrum obtained from the ZnO nanoparticle sample. Two strong peaks are observed at 1021.4 eV and 1044.0 eV, corresponding to the binding energy values for Zn $2p_{3/2}$ and Zn $2p_{1/2}$, respectively. It is interesting to note that the Zn $2p_{3/2}$ peak was centered at 1021.4 eV, shifted towards lower energy from the bulk value of 1022 eV.[23] This peak could be deconvoluted into four peaks, denoted as Za, Zb, Zc, and Zd, which were centered at 1020.7 eV, 1021.2 eV, 1022.0 eV, and 1022.7 eV, respectively, as shown in Fig. 6c.

The peak Zc located at 1022.0 eV corresponds to the XPS binding energy for Zn $2p_{3/2}$ photoelectrons. The presence of peaks other than Zc indicates presence of lattice defects in the ZnO crystal. It has been reported that Zn $2p_{3/2}$ photoelectrons have lower binding energy if they are emitted from a zinc ion present in the vicinity of oxygen vacancy sites.[25,26] Therefore, peaks Zb and Zc located at 1020.7 eV and 1021.2 eV may be contributed by zinc cations situated at oxygen vacancy site.[25–27] The peak Zd positioned at 1022.6 eV may originate from zinc ion present in the vicinity of zinc vacancies.[28]

To confirm the presence of the ZnO shell in the core–shell sample, a narrow-scan spectrum was recorded in the Zn 2*p* region; the result is shown in Fig. 6b. The observed binding energies of the two strong peaks centered at 1021.4 eV and 1044.0 eV are in agreement with the corresponding binding energies of Zn $2p_{3/2}$ and Zn $2p_{1/2}$ photoelectrons, respectively. The Zn $2p_{3/2}$ peaks were further deconvoluted assuming Gaussian line shape; the results are shown in Fig. 6d. This peak could be deconvoluted into four distinct peaks, designated as Za, Zb, Zc, and Zd, at 1020.7 eV, 1021.2 eV, 1022.0 eV, and 1022.8 eV, respectively. All the deconvoluted peaks match with the corresponding values of the deconvoluted peaks Za, Zb, Zc, and Zd for the ZnO nanoparticle sample. Recall that the first two peaks (Za and Zb) originate from oxygen-deficient sites while Zc was attributed to crystalline zinc in ZnO crystal. Our results, therefore, provide conclusive evidence of formation of the core–shell nanostructures. A summary of the relative peak area ratios for Za/Zc and Zb/Zc for bare ZnO and ZnO in the core–shell structure is presented in Table I.

It is interesting to note that, while the binding energies of the Zn $2p_{3/2}$ peaks matched for both the ZnO as well as core–shell sample FZ2, the relative peak area ratios exhibited significant departure. The Za/Zc and Zb/Zc ratios for the core–shell sample FZ2 were much higher compared with the corresponding Za/Zc and Zb/Zc ratios for the bare ZnO

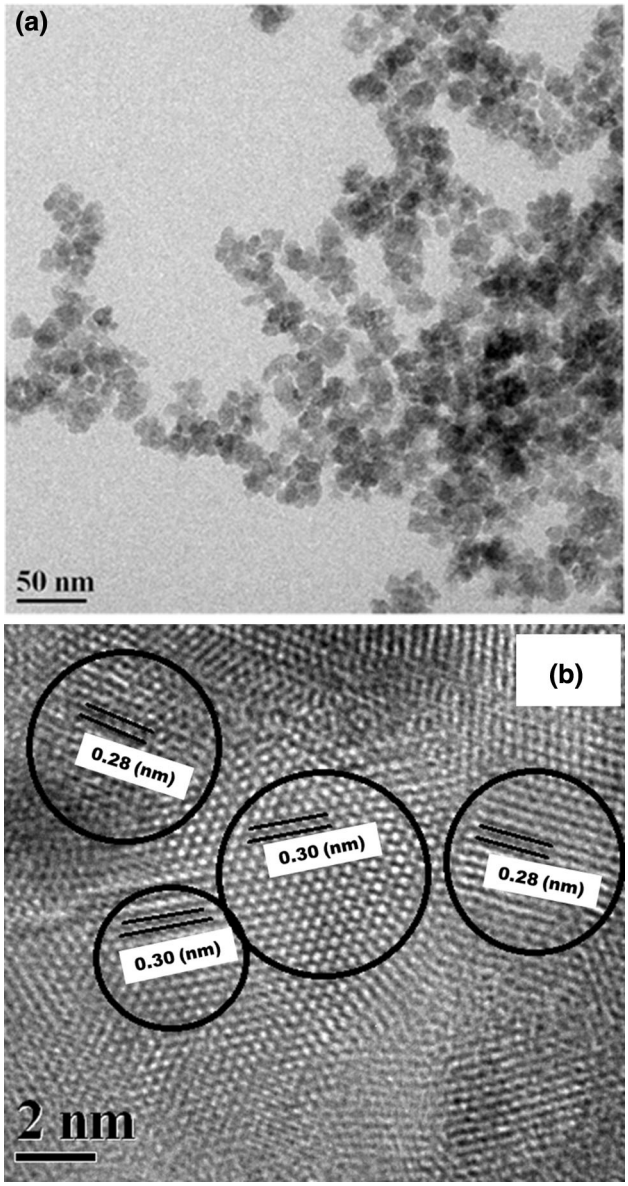

Fig. 4. (a) Electron micrograph of Fe_3O_4–ZnO core–shell nanoparticle sample FZ2. (b) HRTEM pattern of as-synthesized Fe_3O_4–ZnO nanoparticles.

nanoparticles, indicating larger oxygen defect centers in the core–shell samples. A possible explanation for these observations could be the increased surface area of the shell, leading to higher oxygen defect population.

The narrow-scan Fe 2*p* spectra recorded for the core sample F2 and the corresponding core–shell sample FZ2 are shown in Fig. 7a and b, respectively. Note that the photoelectron peaks for the core–shell sample are considerably weaker because of the presence of the ZnO overcoating and the finite escape depth of x-ray photoelectrons. For the Fe_3O_4 sample F2, two distinct binding energy peaks were observed at 710.8 eV and 724.6 eV, in agreement with the respective binding energies for Fe $2p_{3/2}$ and Fe $2p_{1/2}$ of Fe_3O_4.[14,23] The Fe 2*p* peak for the core–shell sample FZ2 is asymmetric. To determine the exact binding energy peak position, the corresponding Fe 2*p* peak was deconvoluted using Gaussian peak fitting. As shown in Fig. 7b, the Fe 2*p* peak observed for the sample FZ2 could be resolved into two distinct peaks, positioned at 710.4 eV and 724.0 eV. The binding energy values were found to shift towards lower energy compared with the corresponding peak positions for the bare core (Fe_3O_4) sample. This red-shift in the binding energy peaks indicates considerable chemical interaction of the iron oxide nanoparticles with Zn atoms of the ZnO shell,[14] hence confirming the coating of the ZnO shell on the Fe_3O_4 nanoparticles.

To further confirm the presence of the ZnO shell in the core–shell nanoparticles, sample FZ2 was sputtered for 4 min followed by XPS reanalysis. Figure 7c presents the narrow-scan spectrum in the Fe 2*p* region after sputtering of sample FZ2. It is interesting to notice that the XPS narrow scan Fe 2*p* peak intensity increased after sputtering, as shown in Fig. 7c. Sputtering of the core–shell sample is expected to increase the elemental concentration of core nanoparticles at the surface. These results thus clearly indicate presence of the ZnO shell over the Fe_3O_4 core nanoparticles.

Optical Characterization

The absorption behavior of all three types of Fe_3O_4 nanoparticles was characterized by a broad absorption feature with no distinct onset, irrespective of the particle size, as shown in Fig. S-2 in the Electronic Supplementary Material. This feature may be due to several factors, viz. Fe^{3+} ligand field transitions or *d*–*d* transitions, intervalence charge transfer, and pair excitations.[29–31] The optical properties of ZnO nanoparticles (7.3 nm), used as the shell material in the core–shell nanostructures, were also studied by UV–Vis absorption spectroscopy. Figure 8 shows the typical optical absorption spectra observed for the ZnO sample and core–shell samples FZ1, FZ2, and FZ3. The absorption spectra of the ZnO nanoparticles exhibited a sharp onset at 362 nm, corresponding to the fundamental absorption edge of the ZnO nanoparticles. Similarly, the core–shell nanoparticle samples FZ1 to FZ3 also exhibited distinct absorption features. The optical absorption onset for sample FZ1, FZ2, and FZ3 was observed at 390 nm, 392 nm, and 390 nm, respectively. For all samples, the thickness of the shell was expected to be the same, approximately 2.3 nm. It is interesting to note that the absorption onset of the core–shell samples shifted towards higher wavelength compared with the corresponding onset of the ZnO sample. It is well known that the absorption properties of ZnO nanoparticles are size dependent due to the quantum confinement effect. Growth of the ZnO shell on the Fe_3O_4 core results in formation of a type 1 core–shell nanostructure with

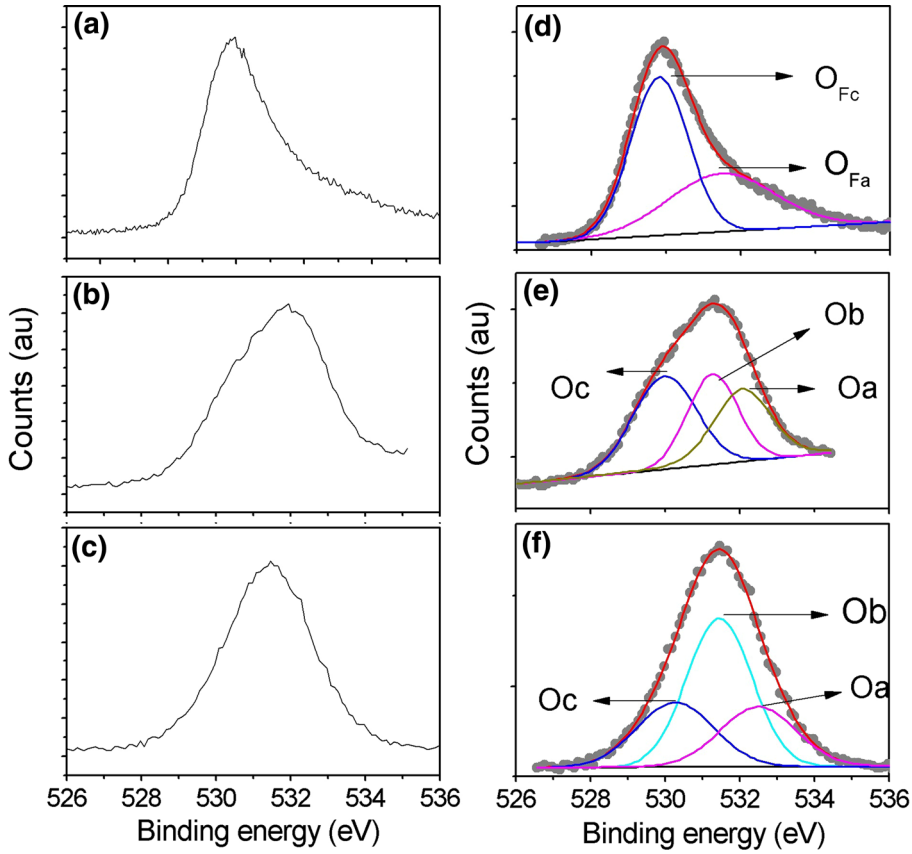

Fig. 5. XPS narrow-scan O 1*s* spectra for (a) F2, (b) ZnO, and (c) FZ2 samples, and (d–f) corresponding deconvolutions.

a wide-bandgap shell and narrow-bandgap core. Such a structure promotes carrier leakage from the shell to core.[32] The red-shift observed in the absorption onset of the core–shell sample vis-à-vis the corresponding onset for the ZnO shell sample may be attributed to such a possibility.

The PL spectra observed for the ZnO, bare core (F2), and core–shell samples FZ1, FZ2, and FZ3 are shown in Fig. 9. The PL spectra for ZnO exhibited an emission band peaking at 380 nm, located close to the absorption onset. This emission peak can therefore be attributed to band-edge emission in ZnO. As expected, the Fe_3O_4 core sample (F2) did not exhibit any PL. However, all three core–shell samples were found to be photoluminescent. The observed PL spectra are obviously due to presence of the luminescent ZnO shell on the Fe_3O_4 core. All the PL emission peaks from the core–shell samples were red-shifted from the corresponding emission peak for the ZnO sample. This red-shift observed in the emission peak may be due to alternate recombination pathways in the core–shell structure.

Magnetic Characterization

The magnetic properties of the as-synthesized core nanoparticle samples were investigated using a superconducting quantum interference device (SQUID) magnetometer at fields up to 7 T at room temperature; the results are shown in Fig. 10a, b, and c for samples F1, F2, and F3, respectively. The absence of any hysteresis in the measured data suggests that all the Fe_3O_4 nanoparticle samples were in superparamagnetic state. The finite size and surface effect may jointly contribute to the observed superparamagnetic behavior. These results are consistent with earlier studies suggesting that magnetic nanoparticles smaller than 16 nm are usually superparamagnetic at room temperature.[13,33] The experimentally determined values of the saturation magnetization (M_s), remanence (M_r), and coercive field (H_c) for Fe_3O_4 samples F1, F2, and F3 at 300 K and 10 K (for F2 only) are summarized in Table II.

The observed saturation magnetization of sample F1 was 9.1 emu/cm^3. However, the corresponding values of M_s for the smaller-sized nanoparticle samples F2 and F3 were found to decrease to 3.26 emu/cm^3 and 2.4 emu/cm^3, respectively. The presence of a capping layer on the nanoparticles may contribute to the observed reduction in the saturation magnetization. The magnetic molecules on the surface lack complete coordination, and the spins may likewise be disordered. Therefore, the large surface-to-volume ratio of nanoparticles may also contribute to the decrease in saturation magnetization.[13] High-field magnetization

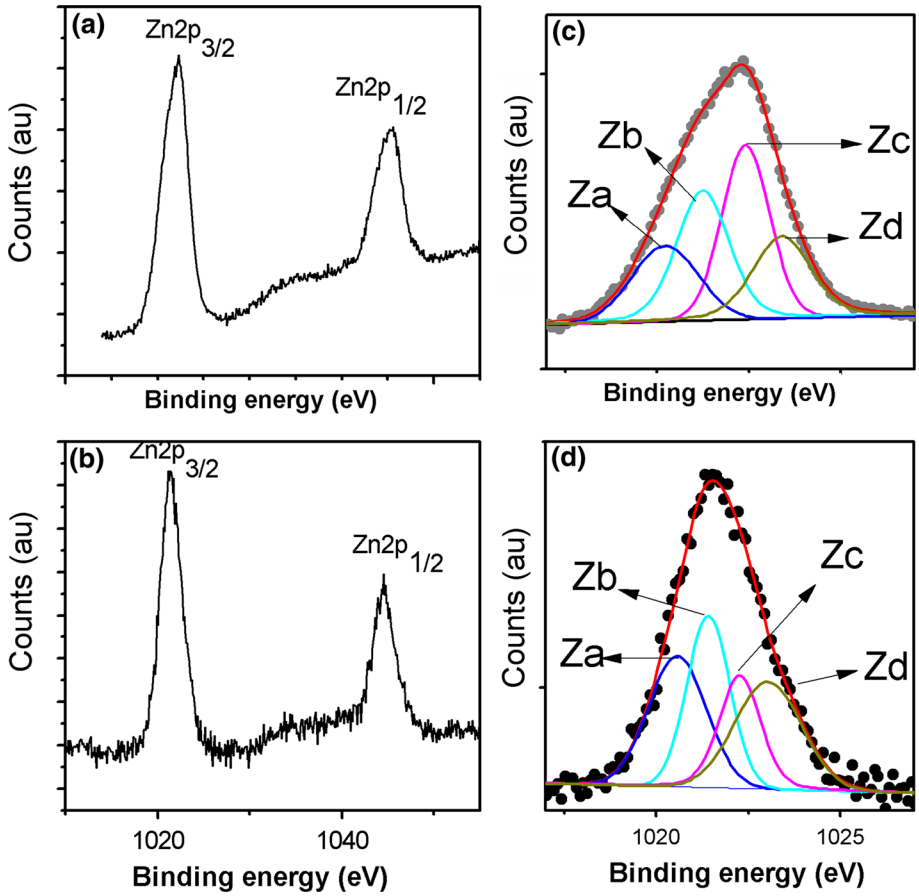

Fig. 6. Zn 2*p* narrow-scan spectra recorded for (a) ZnO nanoparticles and (b) FZ2 core–shell sample, and (c, d) corresponding deconvolutions.

Table I. Observed peak positions and corresponding peak area ratios of Gaussian components of Zn $2p_{3/2}$ peaks for samples of ZnO and Fe_3O_4–ZnO core–shell nanostructures

		Binding energy peak position (eV)				Peak area ratio	
Sample	**Element**	**Za**	**Zb**	**Zc**	**Zd**	**Za/Zc**	**Zb/Zc**
ZnO	Zn $2p_{3/2}$	1020.7	1021.2	1022.0	1022.6	0.74	0.64
FZ2	Zn $2p_{3/2}$	1020.7	1021.2	1022.0	1022.6	1.11	1.23

measurements on γ-Fe_2O_3 and Co nanoparticles have shown that the magnetization is strongly influenced by surface effects, depending on the particle size.[34]

Field-dependent magnetization measurements (M–H curve) at room temperature (300 K) in case of Fe_3O_4–ZnO core–shell samples FZ1, FZ2, and FZ3 are shown in Fig. 11a, b, and c, respectively. Enlarged views of the M–H curves around $H = 0$ are also shown in the insets of Fig. 11a, b, and c for samples FZ1, FZ2, and FZ3, respectively. All the core–shell samples exhibited ferromagnetic behavior, as evidenced by presence of hysteresis and nonzero values of coercive field and remanence. A summary of the measured saturation magnetization (M_s), remanence (M_r), and coercive field (H_c) for all three core–shell nanostructures measured at 300 K and 10 K (for F2 only) is presented in Table III. ZnO nanoparticles exhibit defect-induced ferromagnetism in the small size regime. A possible factor responsible for the ferromagnetism observed in the ZnO nanoparticles at room temperature may be positional defects. Due to the small size of ZnO nanoparticles, strain-dependent oxygen deficiency centers impart ferromagnetism to ZnO nanoparticles.[35–38] Therefore, it can be said that the ferromagnetism observed in the core–shell nanoparticles originates due to the presence of the ZnO shell.

From Table III, it is obvious that the saturation magnetization values determined experimentally for the core–shell nanostructures decreased in comparison with the corresponding values for the bare

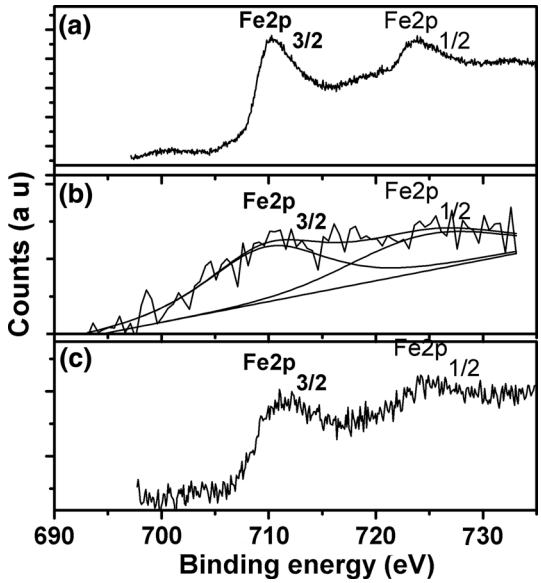

Fig. 7. XPS narrow-scan Fe 2*p* spectra for (a) F2 and (b) FZ2 samples, and (c) typical as-synthesized Fe_3O_4–ZnO core–shell nanoparticles after sputtering.

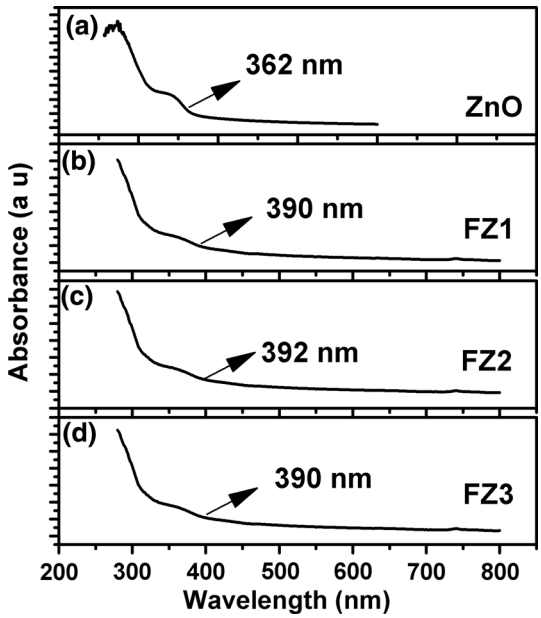

Fig. 8. UV–Vis absorption spectra for (a) ZnO nanoparticles and Fe_3O_4–ZnO core–shell samples (b) FZ1, (c) FZ2, and (d) FZ3.

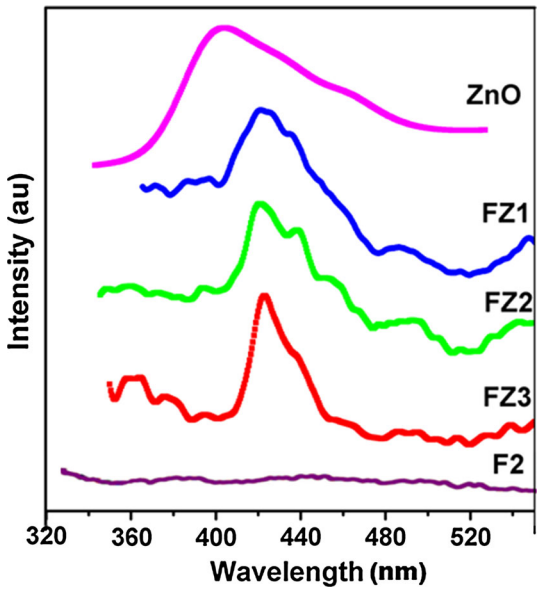

Fig. 9. Room-temperature photoluminescence spectra of as-synthesized ZnO nanoparticles, Fe_3O_4 core sample F2, and Fe_3O_4–ZnO core–shell nanoparticle samples FZ1, FZ2, and FZ3.

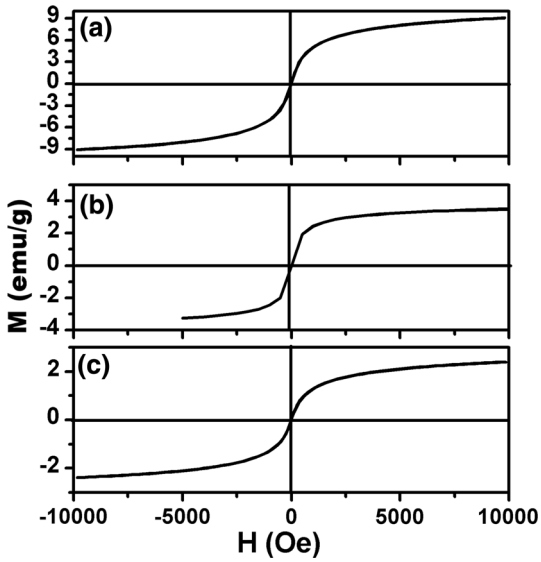

Fig. 10. Experimentally observed magnetic hysteresis at 300 K for Fe_3O_4 nanoparticles (a) F1, (b) F2, and (c) F3.

Fe_3O_4 nanoparticles F1, F2, and F3. The lower values of saturation magnetization for the core–shell nanoparticles may likely be due to the presence of the ZnO shell.

The magnetic properties of the core Fe_3O_4 sample F2 and Fe_3O_4–ZnO core–shell nanoparticle sample FZ2 were also measured at 10 K; the results are shown in Fig. S-3a and b, respectively. Distinctively, a hysteresis loop can be noted for both samples, implying ferromagnetic behavior at 10 K. The saturation magnetization for Fe_3O_4 was found to be 3.86 emu/cm^3. However, the saturation magnetization for the core–shell samples was measured to be 1.05 emu/cm^3, again smaller than the corresponding value for sample F2 measured at 10 K.

The temperature dependence of the zero-field-cooled (ZFC) and field-cooled (FC) magnetization data for sample F2 and the corresponding core–shell sample FZ2 measured at magnetic field of 10 Oe in the range from 2 K to 300 K is shown in Fig. 12. The two curves (FC and ZFC) coincide at higher temperature but begin to separate as the temperature decreases. In the FC measurement, the

Table II. Summary of measured saturation magnetization (M_s), remanence (M_r), and coercive field (H_c) for Fe_3O_4 nanoparticle samples

Sample	Temp. (K)	M_s (emu/cm^3)	M_r (emu/cm^3)	H_c (Oe)
F1	300	9.1	0	0
F2	300	3.26	0	0
	10	3.86	1.21	190.0
F3	300	2.4	0	0
ZnO	300	0.032	7.8×10^{-4}	20.9

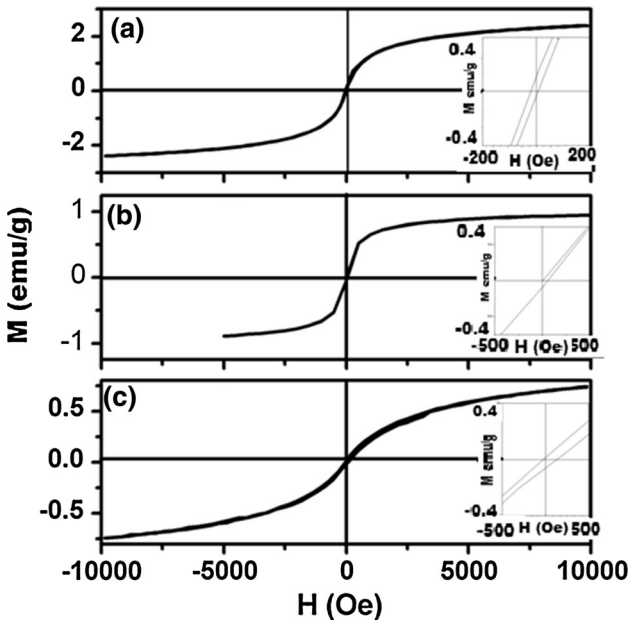

Fig. 11. Field-dependent magnetization at 300 K for Fe_3O_4–ZnO nanoparticle samples (a) FZ1, (b) FZ2, and (c) FZ3. Insets show magnified views of *M*–*H* curves around $H = 0$ Oe.

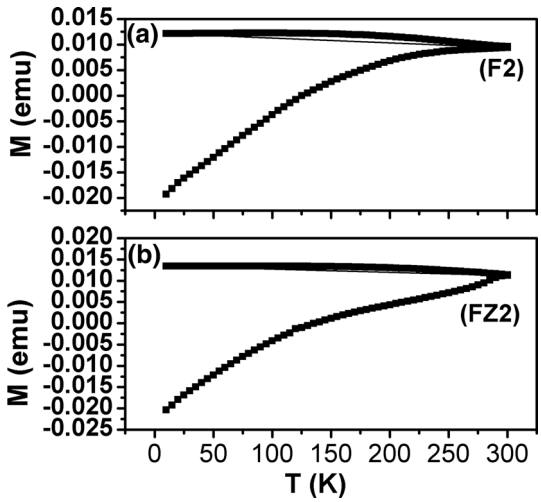

Fig. 12. ZFC and FC curves of as-prepared core Fe_3O_4 and Fe_3O_4–ZnO core–shell samples measured at field of 10 Oe.

Table III. Experimentally determined saturation magnetization (M_s), remanence (M_r), and coercive field (H_c) for Fe_3O_4–ZnO core–shell nanostructures

Sample	Temp. (K)	M_s (emu/cm^3)	M_r (emu/cm^3)	H_c (Oe)
FZ1	300	2.36	4×10^{-2}	8
FZ2	300	0.87	3×10^{-2}	20.0
	10	1.05	20×10^{-2}	139.5
FZ3	300	0.74	1×10^{-2}	12

magnetization increased gradually as the temperature was deceased. At higher temperature, both the FC and ZFC curves for the Fe_3O_4 nanoparticles exhibited the same trend. However, in the case of the ZFC curve, the magnetization decreased when the temperature was decreased below the blocking temperature (T_B). Such behavior is characteristic of superparamagnetism[39] and is due to progressive deblocking of the particle at higher temperature. The blocking temperature (T_B) was measured from the second-order derivative of the curve. The blocking temperature observed for the Fe_3O_4 nanoparticles was found to be 235 K. However, for the core–shell sample FZ2, the magnetization measured under field cooling increased marginally as the sample was cooled. Since the core–shell sample FZ2 exhibited ferromagnetism at room temperature, the value of the blocking temperature was expected to be equal to or greater than room temperature. Accordingly, for the core–shell sample FZ2, the FC and ZFC curves separated from each other at room temperature.

CONCLUSIONS

A multifunctional core–shell nanostructure with an iron oxide core and ZnO shell was successfully grown using a simple room-temperature solution-phase synthesis method. Lattice fringes obtained by HRTEM strongly supported heteroepitaxial growth of the ZnO shell on the magnetic Fe_3O_4 core. SQUID measurements suggested that the Fe_3O_4 core exhibited superparamagnetic properties at room temperature. However, magnetic measurements on the

core–shell nanoparticles suggested ferromagnetic behavior at room temperature. Another noteworthy achievement is the combination of significantly strong optical absorption and photoluminescence behavior with ferromagnetic properties in the as-synthesized core–shell structures. These results thus indicate the interesting possibility of combining magnetic and semiconducting behaviors in a novel way to obtain multifunctionality by designing core–shell nanostructures with a magnetic core and semiconducting shell. Such multifunctional nanostructures may be useful in applications where enhanced magnetic as well as luminescence responses are desired.

ELECTRONIC SUPPLEMENTARY MATERIAL

The online version of this article (https://doi.org/10.1007/s11664-018-6171-3) contains supplementary material, which is available to authorized users.

REFERENCES

1. P. Zhang, B. Wang, G. Williams, C.B. White, J. Quan, and H. Nie, *Mater. Res. Bull.* 48, 3058 (2013).
2. W. Lu, Y. Shen, A. Xie, X. Zhang, and W. Chang, *J. Phys. Chem. C* 114, 4846 (2010).
3. X. You, R. He, F. Gao, J. Shao, B. Pan, and D. Cui, *Nanotechnology* 18, 035701 (2007).
4. V. Salgueirino-Meciera, M.A. Correa-Duarte, M. Spasova, L.M. Liz-Marzan, and M. Farle, *Adv. Funct. Mater.* 16, 509 (2006).
5. J. Xie, C. Xu, Z. Xu, Y. Hou, K.L. Young, S.X. Wang, N. Pourmand, and S. Sun, *Chem. Mater.* 18, 5401 (2006).
6. Z.L. Yang, D.Y. Hua, Z. Ling, G.U.H. Chen, and C. Chin, *Phys. Lett.* 24, 483 (2007).
7. R. Hao, R. Xing, Z. Xu, Y. Hou, S. Gao, and S. Sun, *Adv. Mater.* 22, 2729 (2010).
8. A. Van Dijken, E.A. Meulenkamp, D. Vanmaekelbergh, and M.A. Meijrink, *J. Lumin.* 90, 123 (2000).
9. J. Zhou, Y. Gu, P. Fei, W. Mai, Y. Gao, R. Yang, G. Bao, and Z.L. Wang, *Nano Lett.* 8, 3035 (2008).
10. C.Y. Jiang, X.W. Sun, G.Q. Lo, and D.L. Kwong, *Appl. Phys. Lett.* 90, 263501 (2001).
11. Y. Liu, Y. Zhang, S. Wang, L. Pope, and W. Chen, *Appl. Phys. Lett.* 92, 143901 (2008).
12. C. Hanley, J. Layne, A. Punnoose, K.M. Reddy, I. Coombs, A. Coombs, K. Feris, and D. Wingett, *Nanotechnology* 19, 295103 (2008).
13. J. Joseph, K.K. Nishad, M. Sharma, D.K. Gupta, R.R. Singh, and R.K. Pandey, *Mater. Res. Bull.* 47, 1471 (2012).
14. X.Y. Chu, X. Hong, X.T. Zhang, P. Zou, and Y.C. Liu, *J. Phys. Chem. C* 112, 15980 (2008).
15. Q. Wang, Y. Liu, C. Lin, and H. Yan, *Nanotechnology* 18, 405604 (2007).
16. A. Ito, M. Shinkai, H. Honda, and T. Kobayasi, *J. Biosci. Bioeng.* 100, 1 (2005).
17. M. Mangani, L. Gulluzi, and I.J. Bruce, *J. Nanosci. Nanotechnol.* 6, 2311 (2006).
18. Y.M. Jun, J.S. Choi, and J. Cheon, *Chem. Commun.* 12, 1203 (2007).
19. H. Gu, K. Xu, and B. Xu, *Chem. Commun.* 7, 941 (2006).
20. X. Lu, X. Zhang, Y. Ni, Q. Zhang, and J. Chen, *Biosens. Bioelectron.* 24, 93 (2008).
21. W. Chiu, P. Khiew, M. Cloke, D. Isa, H. Lim, T. Tan, N. Huang, A. Radiman, R. Abd-shukor, M.A.A. Hamid, and C. Chia, *J. Phys. Chem. C* 114, 8212 (2010).
22. K.W. Kwon, B.H. Lee, and M. Shim, *Chem. Mater.* 18, 6357 (2006).
23. D. Briggs and M.P. Seah, Practical Surface Analysis by Auger and Photoelectron Spectroscopy (Wiley, 1990), Appendix-6.
24. S.J. Kang and Y.H. Joung, *Appl. Surf. Sci.* 253, 7330 (2007).
25. K.K. Nishad, J. Joseph, N. Tiwari, R. Kurchania, and R.K. Pandey, *Sci. Adv. Mater.* 7, 1368 (2015).
26. P.T. Hsieh, Y.C. Chen, K.S. Kao, and C.M. Wang, *Appl. Phys. A* 90, 317 (2008).
27. Y.Y. Tay, S. Li, C.Q. Sun, and P. Chen, *Appl. Phys. Lett.* 88, 173118 (2006).
28. A. Kelly, G.W. Groves, and P. Kidd, *Crystallography and Crystal Defects* (New York: Wiley, 2000), p. 289.
29. D.M. Sherman and T.D. Waite, *Am. Mineral.* 70, 1262 (1985).
30. H.J. Schugar, G.R. Rossman, J. Thibeault, and H.B. Gray, *Chem. Phys. Lett.* 6, 26 (1970).
31. Y.P. He, Y.M. Miao, C.R. Li, S.Q. Wang, L. Cao, S.S. Xie, G.Z. Yang, and B.S. Zou, *Phys. Rev. B* 71, 125411 (2005).
32. Y. Matsumoto, *J. Solid State Electron.* 126, 227 (1996).
33. R. Hao, R. Xing, Z. Xu, Y. Hou, S. Gao, and S. Sun, *Adv. Mater.* 22, 2729 (2010).
34. T. Mokari, C.G. Sztrum, A. Salant, E. Rabani, and U. Banin, *Nat. Mater.* 4, 855 (2005).
35. M. Berciu and R.N. Bhatt, *Phys. Rev. Lett.* 87, 107203 (2001).
36. N. Sanchez, S. Gallego, and M.C. Munoz, *Phys. Rev. Lett.* 101, 067206 (2008).
37. X. Xu, C. Xu, J. Dai, J. Hu, F. Li, and S. Zhang, *J. Phys. Chem. C* 116, 8813 (2012).
38. K.K. Nishad and R.K. Pandey, *Mater. Sci. Eng. B* 178, 1380 (2013).
39. J.M.D. Coey, *Phys. Rev. Lett.* 27, 1140 (1971).